

Eccentric Binary Black Hole Simulations with Numerical Relativity

Giuseppe Ficarra^{1,2} and Carlos O. Lousto¹

¹*Center for Computational Relativity and Gravitation,
School of Mathematical Sciences, Rochester Institute of Technology,
85 Lomb Memorial Drive, Rochester, New York 14623, USA*

²*Dipartimento di Fisica, Università della Calabria, Arcavacata di Rende (CS), 87036, Italy*

(Dated: January 17, 2025)

We perform a systematic study of eccentric orbiting nonspinning black hole binaries. We first make a technical study of the optimal full numerical techniques to apply to these studies. We find the grid structure and global resolution that optimize accuracy and speed of current computational resources, while choosing different gauge parameters and Courant factors, $c = dx/dt$, find its optimal value of 0.45. With these choices we perform a study of the merger times $t_m(e)$ as a function of eccentricity, e , for configurations with comparable orbital energy content and find that its dependence is well represented by the post-Newtonian factor $F(e) = (1 + 73e^2/24 + 37e^4/96)/(1 - e^2)^{7/2}$, when merger times are normalized to their quasicircular values, i.e. $t_m(e) \approx t_m(0)/F(e)$. We then perform a systematic coverage of five small-medium eccentricities up to $e \sim 0.45$ and six mass ratios up to 8.5:1 producing a total of 30 simulations covering up to 25 orbits to merger to further model the unequal mass ratio dependence of merger times and as a seed study to a forthcoming new systematic catalog of gravitational waveforms from eccentric binary black holes to allow directly perform parameter estimations of gravitational waves events.

PACS numbers: 04.25.dg, 04.25.Nx, 04.30.Db, 04.70.Bw

I. INTRODUCTION

There is a growing interest in studying highly eccentric binaries, where residual eccentricity persists until close to merger. These eccentric binaries may produce gravitational wave signals that are particularly intriguing and cannot be accurately modeled using quasicircular approximations [1–5]. This subject has attracted considerable attention [6–8], but its detailed modeling remains largely incomplete. Accurate simulations that account for these effects within the sensitivity bands of LISA and third generation detectors can also help to exploit multiband observational opportunities [9–13].

Systematic full numerical simulations of eccentric binaries has been pioneered in [14], and more recently in [15–18]. A recent paper [19] compares definitions of eccentricity [20, 21] during the evolution of full numerical simulations. Long term simulations have also been used to model gravitational waveforms for the inspiral, merger and ringdown of nonspinning moderately eccentric binary black hole systems in [22]. To improve the new modeling [23, 24] of gravitational waves from eccentric long term merging binary black holes, extending thus the intrinsic parameter space to an 8-dimensional one, here we will focus on optimizing the design of full numerical simulations in order to efficiently systematically explore this eccentricity dependence.

The paper is organized as follows, in section II we review the full numerical techniques used throughout this study. We will analyze gains due to increasing the Courant factor and choices of the shift damping parameter. We will also investigate the grid structure and its global resolutions to optimize the computational cost and accuracy of the simulations. In Sec. III we will explore

the dependence of the merger times and number of orbits on the initial eccentricity starting from equivalent total energy configurations of nonspinning equal mass black hole binaries. In Sec. IV we will apply this optimized set ups to produce a first 30 runs catalog of long term simulations and waveforms from nonspinning merging binary black holes covering sparsely unequal comparable mass ratios and up to medium eccentricities. Finally, we will conclude the paper with a discussion section V on how to extend this catalog to additional regions of the parameter space as well as a tighter coverage with yet improved numerical techniques.

II. FULL NUMERICAL TECHNIQUES

In order to perform the full numerical simulations of binary black holes we use the LazEv code[25] which employs 8th order spatial finite differences [26], 4th order Runge-Kutta time integration, and a reduced [27] Courant factor ($c = dt/dx = 1/4$).

For setting up numerical initial data for binary black holes, we regularly adopt the puncture approach [28] along with the TWO-PUNCTURES [29] code. In order to locate apparent horizons during numerical evolutions we use the AH-FINDER-DIRECT [30] and compute horizon masses from its area A_H . Furthermore, we measure the magnitude of the horizon spins S_H , using the “isolated horizon” algorithm [31] as implemented in Ref. [32].

We also use the CARPET [33] mesh refinement driver to pinpoint the evolution of the black holes across the numerical domain. CARPET provides a “moving boxes” style of mesh refinement, where refined grids of fixed size are arranged about the coordinate centers of the holes.

These grids are then moved following the trajectories of the holes during the numerical simulation.

The grid structure of our mesh refinements have a size of the largest box for typical simulations of $\pm 400M$. The number of points between 0 and 400 on the coarsest grid is XXX in nXXX (i.e. n100 has 100 points). So, the grid spacing on the coarsest level is $400/\text{XXX}$. The resolution in the wavezone is $100M/\text{XXX}$ (i.e. n100 has $M/1.00$, n120 has $M/1.2$ and n144 has $M/1.44$) and the rest of the levels is adjusted globally. For comparable masses and non-spinning black holes, the grid around one of the black holes (m_1) is fixed at $\pm 0.65M$ in size and is the 9th refinement level. Therefore the grid spacing at this highest refinement level is $400/\text{XXX}/2^8$. When considering small mass ratio binaries, we progressively add internal grid refinement levels [34]. Here we set units such that $M = m_1^H + m_2^H$ is the addition of the horizon masses.

For the gauge choices, we follow the “moving punctures” approach to dynamically determine coordinates during evolution of the system. Specifically, we use a modified 1+log lapse and a modified Gamma-driver shift condition [35, 36]

$$(\partial_t - \beta^i \partial_i) \alpha = -\alpha^2 f(\alpha) K, \quad (1a)$$

$$\partial_t \beta^a = \frac{3}{4} \tilde{\Gamma}^a - \eta \beta^a, \quad (1b)$$

where typical initial values of the lapse are $\alpha(t=0) = 1/(2\psi_{\text{BL}} - 1)$, where $\psi_{\text{BL}} = 1 + m_{(+)} / (2r_{(+)}) + m_{(-)} / (2r_{(-)})$, and for the shift $\beta^a(t=0) = 0$, with $\eta = 2/M$.

The extraction of gravitational radiation from the numerical relativity simulations is performed using the formulas (22) and (23) from [37] for the energy and linear momentum radiated, respectively, and the formulas in [38] for angular momentum radiated, all in terms of the extracted Weyl scalar Ψ_4 at the observer location $R_{\text{obs}} = 113M$. In order to extrapolate the observer location to infinity, we use the perturbative formulas in Ref. [39]. Fig. 1 provides an illustration of this process of extrapolation in a prototypical eccentric simulation (EcBBH::03 in Table VII, with $e \approx 0.24$ eccentricity) for the $l = m = 2$ mode of the strain waveforms h_+ at different extraction locations $R_{\text{obs}} = 75M - 270M$ compared to the extrapolation to infinity from $R_{\text{obs}} = 113M$.

To quantify the magnitude of the differences between the waveforms due to the finite extraction radii R_{obs} and the extrapolation to infinity, we use the matching measure,

$$\mathcal{M} \equiv \frac{\langle h_1 | h_2 \rangle}{\sqrt{\langle h_1 | h_1 \rangle \langle h_2 | h_2 \rangle}}, \quad (2)$$

as implemented via a complex overlap as described in Eq. (2) in Ref. [40]:

$$\langle h_1 | h_2 \rangle = 2 \int_{-\infty}^{\infty} \frac{d\omega}{S_n(\omega)} \left[\tilde{h}_1(\omega) \tilde{h}_2(\omega)^* \right], \quad (3)$$

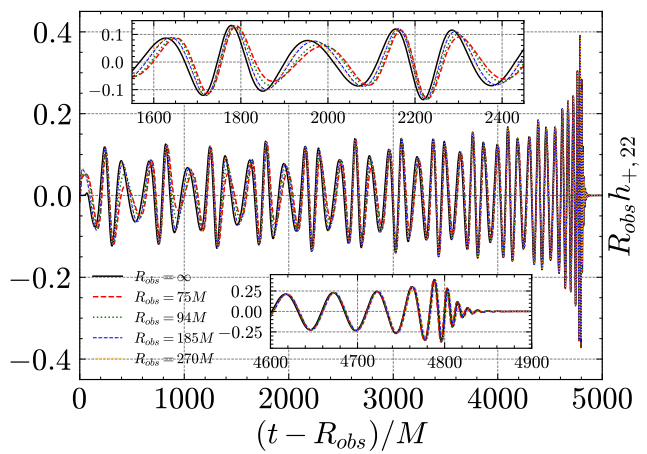


FIG. 1. $l = m = 2$ mode of the strain h_+ waveforms as seen at different extraction radii R_{obs} , and the extrapolated to infinite observer location from the standard choice of $R_{\text{obs}} = 113M$.

where $\tilde{h}(\omega)$ is the Fourier transform of $h(t)$ and $S_n(\omega)$ is the power spectral density of the detector noise (here, taken to be identically equal to one since we are interested in the direct waveforms comparisons). We adopt the leading modes $(\ell, m) = (2, 2)$ of ψ_4 for the computations and we do not maximize over an overall constant time shift and an overall constant phase shift (as is usually done for parameter estimation of gravitational waves signals [41]).

The results are presented in Table I. We observe a monotonic increase in the overlap between the larger extraction radii waveform and that extrapolated to infinity (from the $R_{\text{obs}} = 113M$ waveform). We note here that from the first extraction radius, at $R_{\text{obs}} = 75M$ to $R_{\text{obs}} = 113M$, they lie in an inner refinement level that is our standard extraction zone, that from $R_{\text{obs}} = 126M$ to $R_{\text{obs}} = 185M$ extraction radii are on another external grid refinement level (with half the previous resolution), and the last extraction radii $R_{\text{obs}} = 230M$ to $R_{\text{obs}} = 270M$ at even lower resolutions by a factor $2/3$, all showing the consistency and accuracy of our extraction method. In addition, we performed a new simulation with the same binary parameters and internal refinement levels but extended the two outmost grid levels from $(\pm 200M, \pm 400M)$ to $(\pm 512M, \pm 1024M)$ sizes in order to extract waveforms at $R_{\text{obs}} = 320M, 460M, 496M$ with a spatial resolution of $2M$ in order to approach the scale of the initial orbital period of the binary of about $560M$. The results continue to provide an excellent overlap with the base extrapolated waveform to infinity confirming thus its accuracy when confronted with extractions directly in the radiation zone.

We have also estimated the overlaps of the extrapolated to infinite observer locations themselves to show how those final strain waveforms estimates differ from each other. They are displayed in Table II where we have also arbitrarily split the matching of the full wave-

TABLE I. Matching overlaps at different extraction radii R_{obs} versus the extrapolated to infinite observer location waveform from $R_{obs}/M = 113$

R_{obs}/M	Overlap
75.0	0.979376059
80.0	0.983486543
87.0	0.986744308
94.0	0.989401237
103.0	0.991567460
113.0	0.993377831
126.0	0.994892071
142.0	0.996143412
145.0	0.996332035
170.0	0.997477586
185.0	0.997898820
230.0	0.998473533
250.0	0.998690080
270.0	0.998862511
320.0	0.999264914
460.0	0.999376578
496.0	0.999363088

form into the 'inspiral' part (with frequencies $M\omega \leq 0.1$) and the 'merger' part (with frequencies $M\omega \geq 0.1$), to verify their accuracy separately.

The results seem satisfactory for the present parameter estimation requirements and precision of the planned full numerical simulations.

A. Designing efficient simulations of eccentric binaries

In order to perform our first studies we will consider a reference simulation starting at $r_+ \approx 20M$ with ($e \approx 0.24$ eccentricity) initial data labeled as EccBBH.:03 in Table VII in the Appendix. Then, to improve the performance and accuracy of our simulations, we performed studies involving the time integrations by varying the Courant factor $c = dt/dx$ relating the spatial and time finite difference resolutions, as well as choosing optimal global spatial resolutions and refinement levels to reach acceptable accuracies at the lowest computational price.

We first design a set of simulations that seek improvements in the speed of the simulations by increasing the Courant factor from the conservative $c = 1/4$, adopted since Ref. [27] studies, to the $c = 1/3$ adopted to accelerate the creation of RIT simulations catalogues [17, 42–44], up to the limits of stabilities $c < 0.5$. By choosing to keep the Courant factors constant over all refinements levels to increase the efficiency of the code, we found the stability limits can be increased by choosing a lower shift parameter, from $\eta = 2/M$ down to $\eta = 1/M$ as displayed in Figure 2. We also note here that we have found benefits in the use of the $\eta = 1/M$ gauge when dealing with a quasilocal measure of the black holes recoil [45] and small mass ratio binaries [46, 47]. Finally, we mention that when we remove the outermost refinement level for

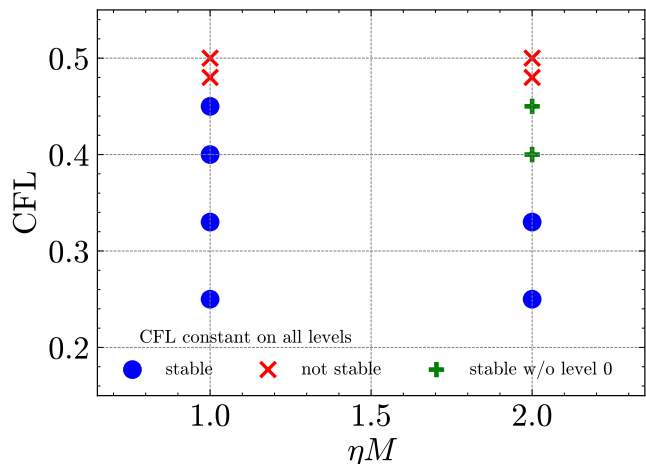


FIG. 2. Stability map of constant Courant factor $c = dt/dx$ through every grid refinement level and for shift evolution parameter η in Eq. (1).

$\eta = 2/M$ (bringing effectively the boundary at 200 or alternatively keeping at 400 with double resolution) we retrieve the stability limit of $\eta = 1/M$, thus showing that the instability is due to underresolution of the outermost simulation grid. These results are consistent with the studies in [27, 46] and the analytic analysis of [48].

We also note that for the typical grids and resolutions used in our simulations, including highly eccentric ones, we observe relatively small differences between the largest stable Courant factor $c = 0.45$ and halving it $c = 0.225$ (even lower than the conservative $c = 0.25$). We display the effects of this variation of the Courant factor in Fig. 3.

We will hence assume the Courant factor $c = 0.45$ and shift damping parameter $\eta = 1/M$ for the rest of the paper. We next focus on the global resolution of the grids to attain both, an efficient and accurate set of simulations with the initial goal to produce a systematic coverage of the parameter space of eccentric nonspinning black hole binaries, and next to be extended to nonprecessing spinning binaries.

In order to start our eccentric binaries simulations we choose the position of the apastron r_+ and parametrize the tangential initial orbital momenta by a fraction $1 - f$ of the circular linear momentum P_c as $P_t = P_c(1 - f)$ [17, 49]. We thus consider a reference nonspinning equal mass binary with initial eccentricity defined by $f = 0.1$ (corresponding to $e = 0.24$) at an initial separation of $r_+ = 20M$ and a grid with 8 refinement levels around each hole.

The results of the evolutions with increasing global resolutions by 1.2 factors labeled as n100, n120, n144, is summarized in Fig. 4 for waveforms and L2-norms of the Hamiltonian violations, both displaying strong convergence rates. We observe the rapid convergence of the merger times towards $4800M$ for n120 and n144, which indicates that n120 provides an accurate enough resolu-

TABLE II. Matching overlaps between extrapolated strain waveforms at infinity computed from different extraction radii. 'Inspiral' and 'merger' split is simply given by $M\omega \leq 0.1$

$(R_1/M, R_2/M)$	(75,113)	(75,185)	(75,270)	(113,185)	(113,270)	(185,270)	(113,496)
full	0.9972	0.9959	0.9956	0.9998	0.9997	0.9999	0.9969
inspiral	0.9491	0.9380	0.9416	0.9982	0.9994	0.9993	0.9884
merger	0.9999	0.9992	0.9968	0.9993	0.9968	0.9990	0.9994

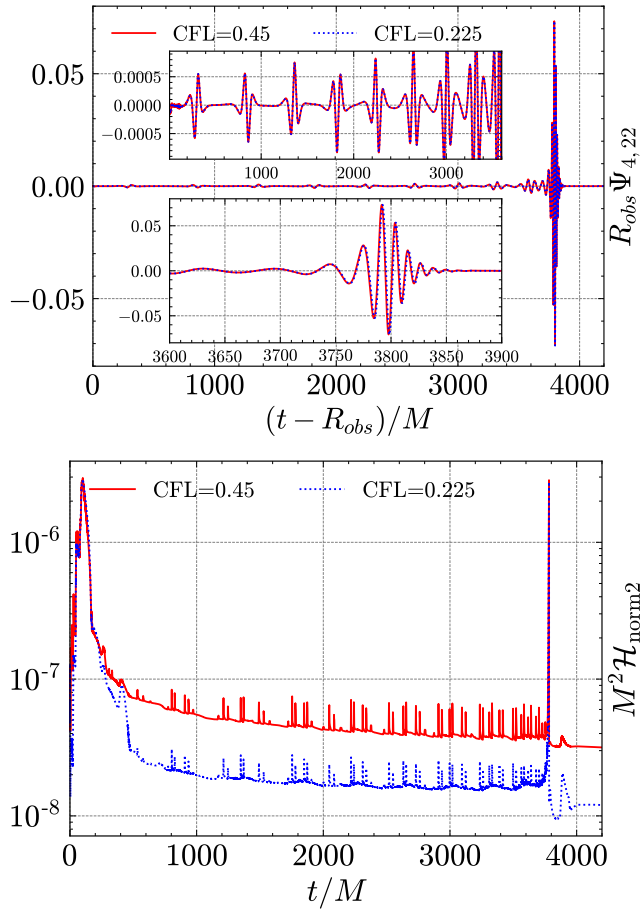


FIG. 3. $l = m = 2$ mode waveform comparison for a prototypical eccentric binary merger (EccBBH:03) by halving the Courant factor. In the lower panel the effects on the L2-norm of the Hamiltonian violations.

tion without needing to incur into the more (twice) computationally expensive n144 simulation. The alternative resolution n100 with 9 refinement levels structure used in previous papers as our preferred standard, leads for instance to a merger time of 4871.9 and a remnant mass of 0.95155345 which improves over n100 with 8 refinement levels but not over n120 with 8 refinement levels, according to Table III results. This preference is indeed corroborated regarding computational efficiency directly by observing the timing of the simulations presented in Fig. 5, performed on 2 compute nodes, each holding 2 Skylake Xeon 6132 CPUs with 14 cores at 2.6GHz and 192GB of RAM. Here we also considered an additional

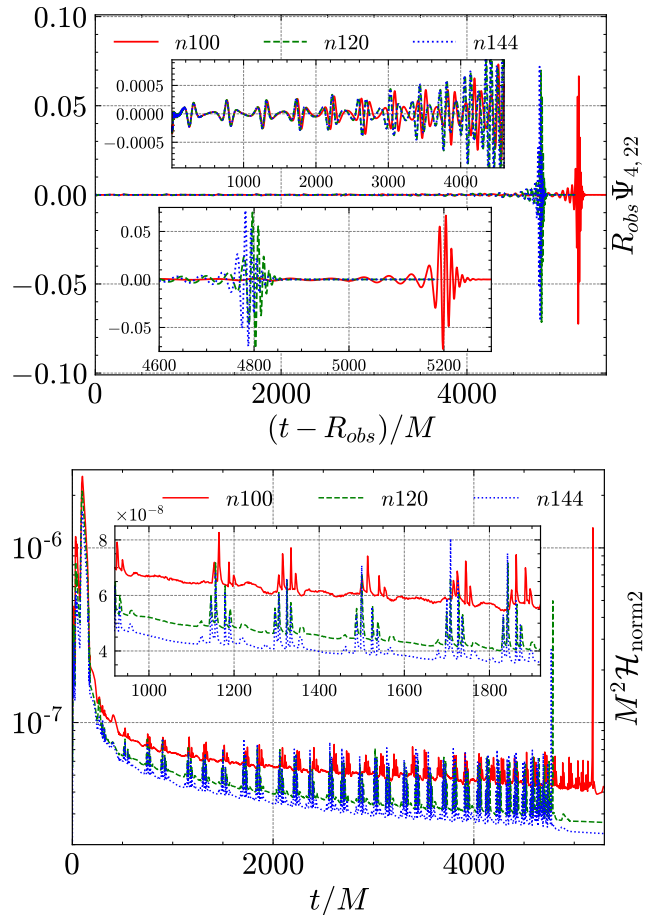


FIG. 4. Global convergence study of an eccentric $e = 0.24$ equal mass nonspinning binary starting from $r_+ = 20M$.

refinement level around the holes at the lowest resolution n100. This again favors the choice of the 8 refinement levels and n120 resolution to become our reference choice for equal mass nonspinning binaries.

III. ECCENTRIC MERGING BINARY BLACK HOLES

With the results of these studies we are ready to select an efficient and accurate numerical setup to perform a series of simulations of black hole binaries, to explore its dependence on eccentricity, as well as on its mass ratios. In the following, we will choose the base global resolution

TABLE III. Convergence of merger time t_m/M , number of orbits N , remnant mass M_f and spin χ_f , strain peak amplitude $(r/M)|h_{22}^{\text{peak}}|$, peak frequency $M\omega_{22}^{\text{peak}}$ and peak luminosity $\mathcal{L}_{\text{peak}}$. Richardson extrapolation is used to determine convergence order and extrapolated values at infinite resolution.

resolution	t_m/M	N	M_f/M	χ_f	$(r/M) h_{22}^{\text{peak}} $	$M\omega_{22}^{\text{peak}}$	$\mathcal{L}_{\text{peak}}[10^{-56} \text{ erg/s}]$
$n100$	5186.70	18.93	0.951749	0.68570	0.391546	0.357027	3.6026
$n120$	4787.63	17.77	0.952027	0.68675	0.393045	0.358207	3.6634
$n144$	4771.56	17.73	0.952045	0.68640	0.392729	0.358488	3.6783
Inf. Extrap.	4770.89	17.72	0.952046	0.68649	0.392784	0.358577	3.6830
Inf. - $n120$	-16.74	-0.05	0.000019	-0.00026	-0.000261	0.000370	1.9606
% difference	0.35	0.28	0.002	0.038	0.066	0.10	0.53
Conv. order	17.62	17.71	15.07	5.99	8.54	7.86	7.74

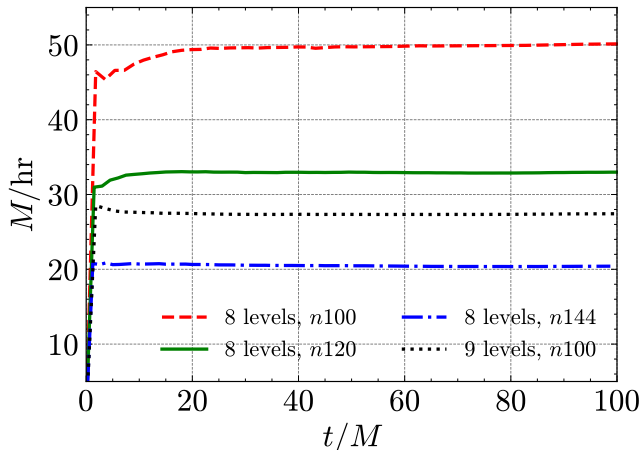


FIG. 5. Timing of simulations on 2 Skylake Xeon 6132 compute nodes.

as $n120$ and 8 refinement levels for equal mass binaries with corresponding increase in the refinement levels on the smaller hole as we consider unequal masses. In all cases we will choose the maximum Courant factor, 0.45, for the gauge with parameter $\eta = 1/M$.

A. Equal mass highly eccentric binary black holes evolutions

When we performed simulations of eccentric binaries from a given initial separation corresponding to the apastron [49], we noticed a strong drop in the number of orbits and time to merger [17] with increasing eccentricity. However, since we generate eccentric orbits by dropping the initial tangential linear momentum P_t by a factor $1 - f$ from the quasicircular one P_c at the apastron, i.e. $P_t = P_c(1 - f)$, the orbits are not energetically equivalent.

While strictly, we can only define a unique eccentricity for Keplerian orbits, at post-Newtonian level it can be generalized by adopting similar looking formulas. Here we adopt the form $r = a_r(1 - e \cos u)$ that has been carried out recently up to 4PN order studies [50].

Now, in order to compare simulations with different eccentricities on a more equal footing, we will consider or-

bits carrying the same “energy”. To illustrate this point, let us see how this can be achieved with Newtonian (or Keplerian) orbits. The apastron can then be defined as $r_+ = a(1 + e)$ while the “energy” of the orbit goes like $E = -M/2a$. Hence, in order to keep the energy of the system fixed for different eccentricities, we need to start at the same values of a rather than r_+ . It turns out that this is also true up to first post-Newtonian order, since a can be expressed as a function of the energy of an eccentric as [50]

$$a_r = \frac{1}{-2E} \left\{ 1 - \frac{E}{2}(\nu - 7) + \frac{E^2}{4} [(1 + 10\nu + \nu^2 + (44\nu - 68)/(-2Eh^2)) + \dots] \right\}, \quad (4)$$

where $\nu = q/(1 + q)^2$ and in the last term we can replace $-2Eh^2 = (1 - e^2)$ at this 2PN order term (Here h is given by $h = J/(GM)$ with J being the orbital angular momentum per unit reduced mass).

This allow us to find the initial separation of our simulations as $r_+ = a_r(1 + e)$ for families of fixed E values varying the eccentricity e . Note though that, due to the 2PN eccentricity dependence $\sim 1/(1 - e^2)$, Eq. (4) breaks down for high values of e , while for small values goes like $\sim e^2$. We have thus designed a sequence of nonspinning equal mass simulations with varying eccentricities parameterized by the tangential factor $f(e) = 1 - P_t/P_c$, while keeping the reference a_r constant, as displayed in Table IV. Here we provide a mapping between the more precise eccentricity estimate of the full numerical simulations e from the 3.5PN approximation as computed in [49] and the simpler Newtonian relation $e_N = 2f - f^2$, providing the leading dependence, for comparison.

Given that in Eq. (4) the 2PN eccentricity dependence diverges for $e \rightarrow 1$, as a sanity check, we have used explicitly the headon collision case expression in the Arnowitt-Deser-Misner transverse-traceless (ADM TT) gauge, from Eq. (3.18) in Ref. [51],

$$\epsilon/\mu = E = -\frac{M}{r} \left(1 - \frac{1}{2} \frac{M}{r} + \frac{1}{4} (1 + 3\nu) \frac{M^2}{r^2} + \dots \right), \quad (5)$$

and equated this to the circular 2PN energy in Eq. (4) with our reference $a_r = 16.04418656$. We find that they

TABLE IV. Initial separation of equal mass binaries for different eccentricities

f	e_N	e	a_r/M	r_+/M
0.00	0.00	0.00	16.04418	16.04418
0.05	0.0975	0.1242	16.04418	18.03701
0.10	0.1900	0.2393	16.04418	19.88372
0.15	0.2775	0.3463	16.04418	21.60086
0.20	0.3600	0.4452	16.04418	23.18787
0.25	0.4375	0.5350	16.04418	24.81825
0.30	0.5100	0.6156	16.04418	25.92176
0.325	0.5444	0.6509	16.04418	26.48786
0.35	0.5775	0.6825	16.04418	26.99510
0.40	0.6400	0.7342	16.04418	27.82454
0.50	0.7500	0.8007	16.04418	28.89190
0.60	0.8400	0.8419	16.04418	29.55227
0.70	0.9100	0.8739	16.04418	30.06557
0.80	0.9600	0.9041	16.04418	30.55021
0.90	0.9900	0.9395	16.04418	31.11799
0.95	0.9975	0.9662	16.04418	31.54632
1.00	1.0000	1.00	16.04418	32.08837
1.00	1.0000	headon	17.67086	35.34172

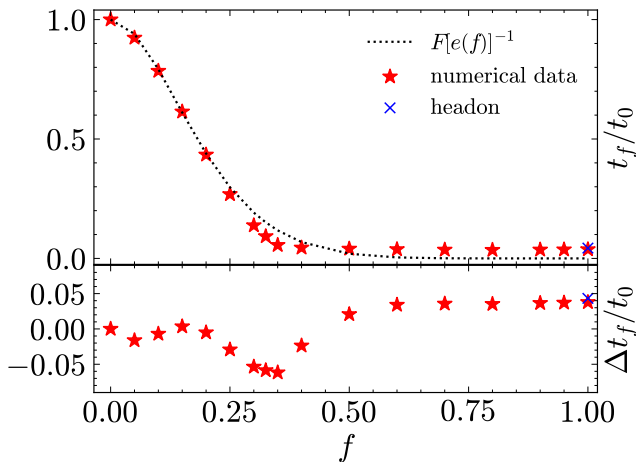


FIG. 6. Merger times by the systems with different eccentricity normalized to the merger times by the quasicircular reference case as a function of f . Bottom panel shows the residuals to the predicted dependence $F(e)$ in Eq. (6).

match for $r_+ = 35.34172060$, which gives an alternative to the one used in our 1PN sequence. This value is displayed at the bottom of Table IV and in Fig. 6, showing the robustness of our approximations and estimates.

The merger times of these simulations t_f as a function of our parametrization of the eccentricity f are displayed in Fig. 6, normalized to the quasicircular merger time t_0 . Again, these display the strong decrease of merger times with increasing eccentricity, this time from nearly equivalent 'energy' content. Notably, we find that the low-medium eccentricity regime, $f \leq 0.25$, seems to follow the enhancement factor, Eq. (6), of [52],

$$F(e) = \frac{(1 + 73e^2/24 + 37e^4/96)}{(1 - e^2)^{7/2}}. \quad (6)$$

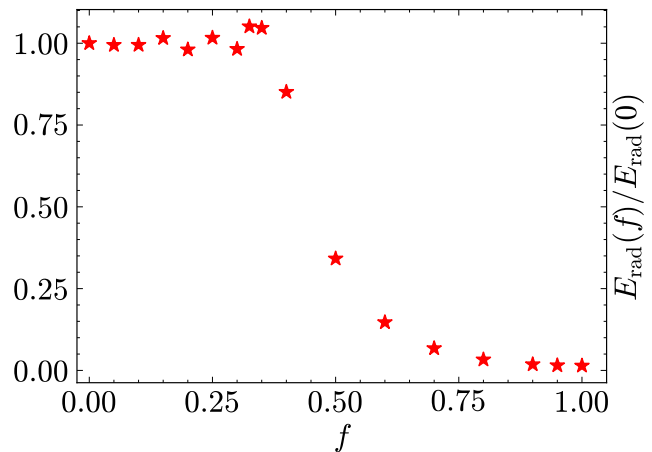


FIG. 7. Radiated energy by the systems with different eccentricity normalized to the energy radiated by the quasicircular reference case as a function of f .

In drawing these plots, for the sake of consistency with this low PN order, we have used the Newtonian relation $e = 2f - f^2$.

The expected leading behavior for the merger time can be obtained from Eq. (5.6) of [53]

$$\langle da/dt \rangle = -\frac{64\nu}{5(a/M)^3} F(e), \quad (7)$$

and upon integration over the a -dependence and time-dependence. Since we start all simulations at the same $a = a_r$, the ratio of the eccentric case to the circular one ($F(0) = 1$) will simply be $t(e) = t(e = 0)/F(e)$. This is closely to what we observe in Fig. 6, where we also plot the residuals of the full numerical merger times to this $F(e)$ -dependence normalized to the merger time. Notably, they lie within a $\sim 5\%$ and they can be used to display the regime of validity of this approximation, to small-medium eccentricities reaching up to values of $e \approx 0.5$.

We can also study the energy radiated versus the eccentricity for our family of simulations in Table IV. The results are displayed in Fig. 7, where we observe a certain constancy of the energy radiated versus eccentricity for, again, low-medium values of e , ie. up to values of $f \approx 0.35$, before the values drop due to plunge dominated orbits.

This low-medium e behavior can be found from Eq. (5.4) of Ref. [53]

$$\langle dE/dt \rangle = -\frac{32\nu^2}{5(a/M)^5} F(e), \quad (8)$$

which upon taking the ratio with respect to the circular case and using that time-dependence of $t(e) = t(e = 0)/F(e)$, leads to $E_{rad}(e)/E_{rad}(0) = F(e)t(e)/(F(0)t(0)) = 1$, which describes roughly the observed constant behavior for $f \leq 0.35$ in Fig. 7, ie. for small to medium eccentricities, not directly plunging.

Notably there seems to be a transition from inspiral to direct merger for intermediate values of f (or e). We can explore this further by taking the ratio of Eqs. (8) and Eq. (5.7) of Ref. [53]

$$\langle de/dt \rangle = -\frac{304M^3\nu}{15a^4} e \frac{(1 + 121e^2/304)}{(1 - e^2)^{5/2}}, \quad (9)$$

to obtain

$$\frac{dE_{rad}}{de} = \frac{6}{19} \frac{M^2\nu}{a} \frac{(1 + 73e^2/24 + 37e^4/96)}{e(1 - e^2)(1 + 121e^2/304)}, \quad (10)$$

and to find an inflection point in the behavior $E(e)$ by taking a further derivative of Eq. (7) and equating to zero. We then find

$$\frac{d^2E_{rad}}{de^2} = 0; \quad e_i = 0.6054. \quad (11)$$

Tracing this back to the corresponding Newtonian relation $f_i = 1 - \sqrt{1 - e_i}$, leads to $f_i = 0.3718$, which notably lies near the transition observed in Fig. 7.

It is also interesting to note here that in the radiated energy displayed in Fig. 7 there seems to be superposed oscillations of growing amplitude as we approach the transition values of the eccentricity ($f(e_i)$). These oscillations are reminiscent of what occurs near critical phenomena in phase transitions, here separating the orbital from the direct merger phases. This is beyond the scope of the current paper and deserves a new exploration in its own with new targeted fine tuned simulations.

B. Additional studies

Here we will explore two additional questions with our eccentric simulations. One is regarding the possibility of excitation and amplification of the black hole quasinormal modes at the closest passage around the periastron. Note that this kind of phenomena has been observed for the fundamental mode of neutron stars binaries [54]. However, black holes are much more stiffer and it was already observed with early simulations that they, for instance, do not tidal lock at the latest merger stages [55].

In order to visualize this effect in our reference simulations, we have extracted the spectrum of radiation of the 4th, 5th, and 6th, closest passages (out of the total 17 periastron passages down to merger), from the highest resolution, n144, waveform on top of Fig. 4. In Fig. 8 we show the results of isolating the radiation of those three successive passages and we see that their spectrum is clearly peaked at low frequencies, corresponding to a wavelength of the size of the separation of the closest approach, thus being dominated by the orbital radiation of gravitational waves, rather than by the quasinormal modes of the individual holes, that seem to be completely overshadowed by the orbital radiation. In order to cross check this effect, we have also computed the spectrum of

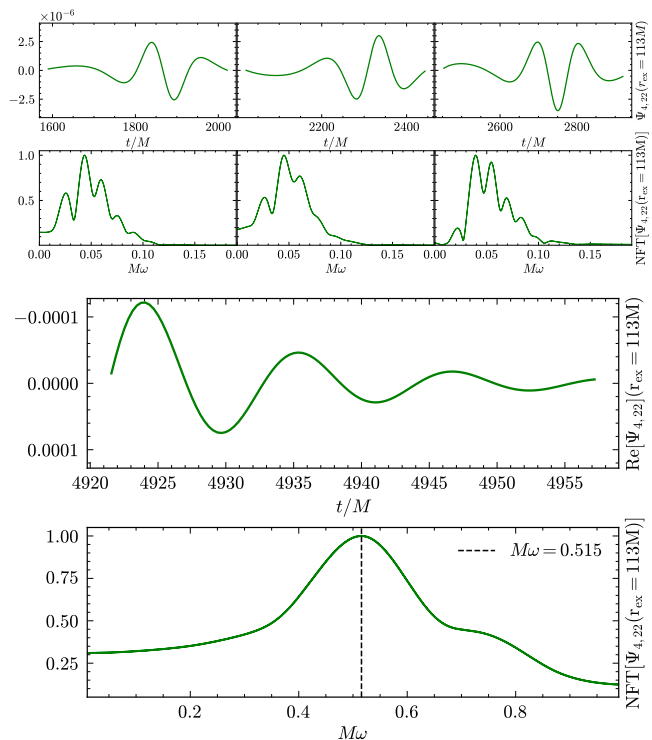


FIG. 8. On top the isolated radiation during successive passages through the periastron and its corresponding spectrum. On the bottom the final black hole quasinormal ringing and corresponding spectrum. Note the order of magnitude differences in the characteristic frequencies.

the final black hole quasinormal ringing, showing clearly that the characteristic frequency is an order of magnitude higher than what we observed during the periastron passages.

The second observation is that, while our standard set up to initiate eccentric simulations benefits of the location of the periastron, it is of interest to generalize it to the case of starting from the apastron. In that case, our choice of the tangential initial linear momentum $P_t = (1 - f)P_c$, as a fraction of the quasicircular momentum P_c for $0 \leq f \leq 1$, can be extended to negative values of f that would lead to eccentric orbits from the periastron, for sufficiently small negative values, and to hyperbolic encounters, for larger negative values of f . These configurations are depicted in Fig. 9 where we can observe that starting the simulations with positive $f \leq 1$ as is our standard, one can diminish its values to $f = 0$ for the quasicircular orbit and then move the focus of the ellipse closer to the starting coordinate of the hole with $f \leq 0$, thus transitioning to a periastron initial configuration.

We performed five simulations with values of $f = -0.05, -0.2, -0.15, -0.2, -0.25$ and computed the merger times to the quasicircular case as displayed in Fig. 10. In order to relate to the corresponding positive values of f we corrected by the first half orbit flying time

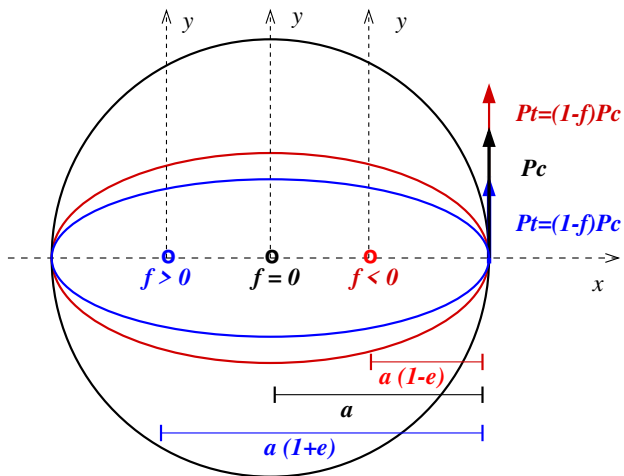


FIG. 9. Initial configurations for binaries starting from apastron or periastron.

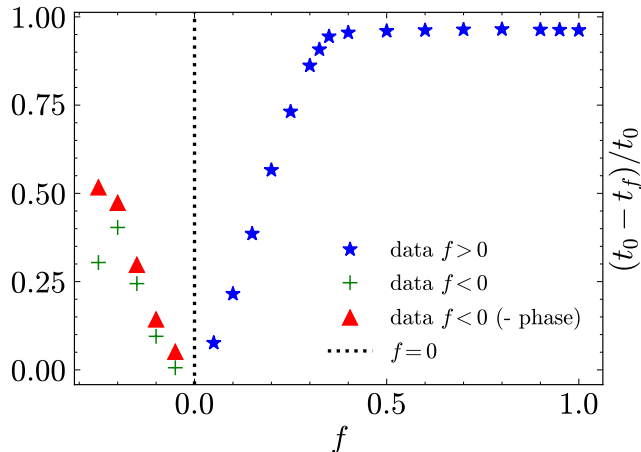


FIG. 10. Merger times for eccentric orbits with reference to the quasicircular case for simulations starting from apastron $f > 0$ and periastron $f < 0$. Correction of the flying time from periastron to apastron (-phase) leads to a more symmetric behavior around $f = 0$ as expected for small e .

from periastron to apastron. This leads to a more symmetric behavior of the merger time versus f as expected for small eccentricities, since once reached the periastron this would put us on an equivalent $-e \rightarrow +e$ orbit. In fact, when we correct for this orbital phase we find a 'V' shape behavior of the merger times as expected.

We have also verified that the radiated energy for those small $f < 0$ cases remains relatively constant as predicted for $f > 0$ and displayed in Fig. 7.

As we mentioned, larger negative values of f would lead to hyperbolic orbits. In order to visualize when roughly this occurs, one can resort to the Newtonian relationship $e_N = 2f_N - f_N^2$, that leads to the critical $e = -1$ value for $f_N(-1) = 1 - \sqrt{2} = -0.4142$.

IV. UNEQUAL MASS ECCENTRIC BINARY BLACK HOLES EVOLUTIONS

Here we will perform a series of simulations to systematically cover (sparsely, for the moment) the parameter space of eccentric, unequal (comparable) nonspinning black hole binaries. This will serve as a seed for a more thorough coverage of the (in principle 8-dimensional) parameter space of the binaries. In doing so we will use the optimized techniques studies presented in Sec. II A.

To choose the unequal mass configurations we will consider equal spacing, not in the mass ratio $q = m_1/m_2$ but rather in the symmetric mass ratio $\nu = q/(1+q)^2$ and restrict to comparable mass ratios $q > 1/10$. We will thus consider the sequence $4\nu = i/8, i = 8.3$, thus leading to values of $q = 1, 0.47759225, 1/3, 0.2404082058, 0.1715728752, 0.1169631198$. Taking our base grid of 8 refinement levels for each hole in the equal mass case, we add one refinement level for the $q = 0.47759225$ case around the smaller hole, and another one for the $q = 1/3, 0.2404082058$ cases, finally reaching 8+11 refinement levels for the $q = 0.1715728752, 0.1169631198$ cases.

The second choice has to do with the fact that starting the simulations at the same initial separation (or same a_r) leads to much larger merger times simply due to the fact that small mass ratios radiate much less gravitational energy $\approx \nu^2$. In order to compensate in part for this effect we consider the leading decay behavior of the orbit in a post-Newtonian expansion, ie. $\dot{r} \approx -(64/5)\nu(m/r)^3$ for quasicircular orbits [56]. This leads us to choose the $a_r(\nu) = a_r(q=1)(i/8)^{1/4}, i = 8.3$ for our choice of symmetric mass ratios. This sequence leading to the following decreasing values of a_r for decreasing mass ratios, $a_r(\nu)/M = 16.04418656, 15.51742720, 14.93079797, 14.26552330, 13.49149896, 12.55525449$.

The combined sequences of 6 mass ratios and 5 eccentricities (parametrized by the reduction factor f) is given in Table V, where we have computed the eccentricity e from f using the 3.5PN formulas in [49] and used the same a_r for a fixed value of each mass ratio q . We did not correct for the different decay times due to eccentricity by the enhancement factor [52, 53], since this will allow us to further verify the e -dependence in the unequal mass cases and extend it to higher order corrections in ν .

Notably, Fig. 11 displays an excellent agreement between the leading $F(e)$ -dependence for equal mass binaries. We also observe an increasing residual for decreasing mass ratio binaries and for higher eccentricities.

In order to model these residuals observed in Fig. 11 we resource to the studies in Ref. [57] for the flux Eq. (2.1) and in particular the term in Eq. (2.37), where a correction to the gravitational radiation flux due to the mass octupole takes the form

$$R_1^{MO} = \frac{(1-4\nu)}{(1-e^2)^{9/2}} \left[\frac{1367}{1008} + \frac{18509}{2016} e^2 + \mathcal{O}(e^4) \right], \quad (12)$$

that we will consider as the leading 1PN dependence for

TABLE V. Initial separation of unequal mass binaries for different eccentricities

4η	$1/q$	a_r/M	f	e	r_+/M
8/8	1.0	16.04418	0.00	0.0	16.04418
			0.05	0.1242	18.03701
			0.10	0.2393	19.88372
			0.15	0.3463	21.60086
			0.20	0.4452	23.18787
7/8	2.093836	15.51742	0.00	0.0	15.51742
			0.05	0.1251	17.45910
			0.10	0.2410	19.25782
			0.15	0.3484	20.92411
			0.20	0.4473	22.45870
6/8	3.0	14.93079	0.00	0.0	14.93079
			0.05	0.1261	16.81455
			0.10	0.2427	18.55584
			0.15	0.3506	20.16664
			0.20	0.4493	21.64016
5/8	4.159591	14.26552	0.00	0.0	14.26552
			0.05	0.1273	16.08232
			0.10	0.2449	17.75931
			0.15	0.3530	19.30187
			0.20	0.4512	20.70245
4/8	5.828427	13.49149	0.00	0.0	13.49149
			0.05	0.1286	15.22752
			0.10	0.2471	16.82567
			0.15	0.3554	18.28638
			0.20	0.4525	19.59700
3/8	8.549703	12.55525	0.00	0.0	12.55525
			0.05	0.1301	14.18857
			0.10	0.2493	15.68615
			0.15	0.3572	17.04116
			0.20	0.4524	18.23601

our residuals modeling. We note that the complete 1PN correction, Eq. (548b) of Ref. [58] would lead to the same leading dependence for our residuals.

From

$$\Delta = [dE/dt(e, \nu) - dE/dt(e, 4\nu = 1)] / [dE/dt(e = 0, \nu)], \quad (13)$$

that we will use in a low eccentricity expansion to model the unequal mass correction to the merger time,

$$[t(e, \nu) - t(e, 1/4)] / t(0, \nu) \approx \Delta, \quad (14)$$

where

$$\Delta = (1 - 4\nu)(Ae^2 + C); \quad e_N^2 = (2f_N - f_N^2)^2. \quad (15)$$

where $A = 7703M/504a_r$ and $C = 1367M/1008a_r$ for this 1PN octupole correction, but which we will take them freely as fitting parameters to the full numerical simulations.

The results of these fits for each mass ratio sequence are displayed in Fig. 12.

For the sake of completeness we provide here the fitting values found for these simulations in Table IV as A_N and C_{NR} , and where we compare those values with the corresponding 1PN predictions $A_{1PN} = 7703M/504a_r$

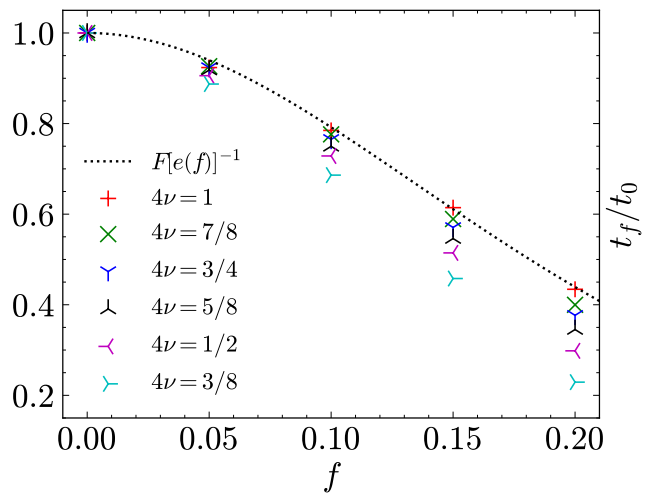


FIG. 11. Merger time for unequal mass ratio binaries and residuals to the equal mass cases.

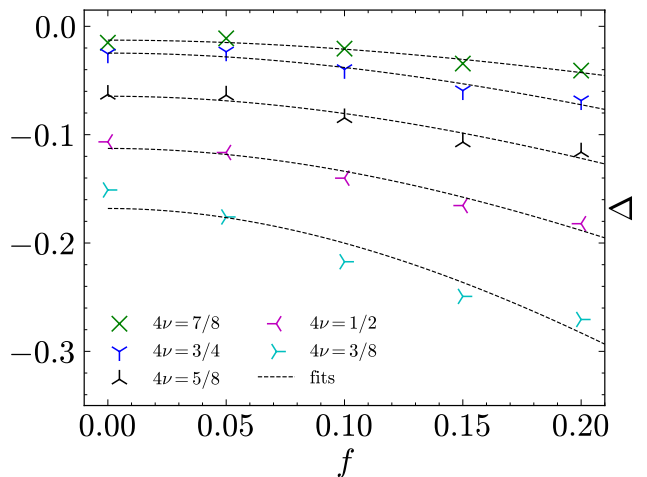


FIG. 12. Fitting to the merger time correction for unequal mass ratio binaries.

and $C_{1PN} = 1367M/1008a_r$, finding good agreement. Note that the fitted C also includes residual corrections due to the different $e = 0$ starting a_r for different mass ratio simulations.

Collecting the results of equal and unequal mass binaries, we have an approximate predictive formula for the merger time t_m of eccentric to quasicircular orbits of the

TABLE VI. Fit results for the modeling defined in Eq. (15).

4ν	A_{NR}	C_{NR}	A_{1PN}	C_{1PN}
7/8	1.849 ± 0.270	0.013 ± 0.002	0.98494	0.08739
6/8	1.471 ± 0.194	0.025 ± 0.003	1.02363	0.09083
5/8	1.179 ± 0.175	0.065 ± 0.005	1.07137	0.09506
4/8	1.168 ± 0.145	0.113 ± 0.005	1.13284	0.10051
3/8	1.418 ± 0.261	0.168 ± 0.011	1.21731	0.10801

form

$$t_m(e, \nu)/t(e=0, \nu) = 1/F(e) + (1 - 4\nu)(A - \frac{157}{24}C)e^2, \quad (16)$$

where $F(e) = (1 + 73e^2/24 + 37e^4/96)/(1 - e^2)^{7/2}$, and for the 1PN approximation, which approximately matches the full numerical values as seen in Table IV, we have $(A - \frac{157}{24}C) = (155125 M)/(24192 a_r)$.

V. CONCLUSIONS AND DISCUSSION

With the goal of producing a thorough catalog of eccentric binaries, we have first made a comparative study of full numerical parameters to optimize the efficiency of such runs in a prototypical case. We have thus found new options to our standard of simulations to generate catalogs, including an increase in the Courant factor to 0.45 that can be carried out to all refinement levels provided we use $M\eta = 1$ for the damping parameter of the shift evolution. We also found that it is more accurate and efficient to trade a refinement level around black holes for a global 1.2 factor increase in the resolution of the grids.

We used this optimized full numerical set up to make a first thorough study of nonspinning equal mass merging binaries versus initial eccentricity to find that the decrease in the merger time and number of orbits could be very well modeled by the leading Post-Newtonian factor $F(e) = (1 + 73e^2/24 + 37e^4/96)/(1 - e^2)^{7/2}$, when values are normalized by the full numerical quasicircular, $e = 0$, case. Note that the normalization of $t_m(e)/t_m(e=0) = 1/F(e)$ is very important as this is done by a full numerical simulation to compute $t_m(e=0)$ instead of using the 1PN estimate, for instance from Eq. (7), thus avoiding the simple prefactor $-(64\nu)/(5(a/M)^3)$ to estimate the merger time of a quasicircular orbit.

The base grid was then scaled to unequal mass ratio binaries by increasing the number of refinement levels around the smaller hole [34], what allowed us to make a first study of the mass ratio ν -dependence, finding a modeling for the corrections to the merger times due to unequal masses and small-medium eccentricities. This in turn can be used to better estimate a priori how to simulate comparable length waveforms to consistently populate moderately eccentric binary black hole merger catalogs. For larger eccentricities it would be interesting to incorporate the modeling of [59, 60].

The success of these simulations and its modeling encourage to produce further studies of eccentric binaries extending them to spinning binaries as well as to improve the coverage in length and mass ratios to be used in parameter estimation studies (as for instance done in [61]) and in model developing. Those simulations are to be made public in the RIT BBH waveforms catalog <https://ccrpages.rit.edu/~RITCatalog/>.

ACKNOWLEDGMENTS

The authors thank Manuela Campenelli, Michail Chabanov, Alessandro Ciarfella, Lorenzo Ennoggi, James Healy, Hiroyuki Nakano, and Yosef Zlochower for many useful discussions. The authors also gratefully acknowledge the National Science Foundation (NSF) for financial support from Grant PHY-2207920. Computational resources were also provided by the Blue Sky, Green Prairies, and White Lagoon clusters at the CCRG-Rochester Institute of Technology, which were supported by NSF grants No. AST-1028087, No. PHY-1229173, No. PHY-1726215, and No. PHY-2018420. This work used the ACCESS allocation TG-PHY060027N, founded by NSF, and project PHY20007 Frontera, an NSF-funded Petascale computing system at the Texas Advanced Computing Center (TACC).

Appendix A: Initial data and results Tables

In Table VII a small P_r component has been added to the initial quasicircular parameters from the instantaneous dP/dt up to 3.5PN radiation terms [62, 63] in order to ensure a lower eccentricity. In all other explicit eccentric cases the prescription consists on setting $P_r = 0$ [49].

In Table VIII we provide the merged black hole properties, final mass, spin and recoil velocity of the remnant hole. We also provide a measure of the radiated gravitational energy, consistent with the final mass of the merged hole and waveform properties such as the peak luminosity, amplitude and frequency of the leading (2,2)-mode. The time and number of orbits to merger of our simulations completed the table. These properties are given in the format of the metadata in the RIT BBH waveforms catalog <https://ccrpages.rit.edu/~RITCatalog/>.

TABLE VII. Initial data parameters for the sequence of simulations described in Sec.IV with a larger black hole (labeled 1) and a smaller black hole (labeled 2). Punctures are located at $\vec{r}_1 = (x_1, 0, 0)$ and $\vec{r}_2 = (x_2, 0, 0)$ with symmetric mass ratio ν , eccentricity parameter f , linear momenta $P = \pm(P_r, P_t, 0)$, puncture masses m^p/M , horizon (Christodoulou) masses m^H/M and total ADM mass M_{ADM}/M .

Run	x_1/M	x_2/M	4ν	f	P_r/M	P_t/M	m_1^p/M	m_2^p/M	m_1^H/M	m_2^H/M	M_{ADM}/M
EccBBH::01	8.02	-8.02	1	0.00	-2.09e-04	0.07064	0.4912	0.4912	0.5000	0.5000	0.9931
EccBBH::02	9.00	-9.00	1	0.05	0.0000	0.06253	0.4923	0.4923	0.5000	0.5000	0.9930
EccBBH::03	9.94	-9.94	1	0.10	0.0000	0.05577	0.4931	0.4931	0.5000	0.5000	0.9930
EccBBH::04	10.85	-10.85	1	0.15	0.0000	0.05001	0.4938	0.4938	0.5000	0.5000	0.9931
EccBBH::05	11.68	-11.68	1	0.20	0.0000	0.04506	0.4943	0.4943	0.5000	0.5000	0.9931
EccBBH::06	5.02	-10.50	7/8	0.00	-1.79e-04	0.06314	0.6691	0.3150	0.6768	0.3232	0.9938
EccBBH::07	5.64	-11.82	7/8	0.05	0.0000	0.05575	0.6701	0.3160	0.6768	0.3232	0.9937
EccBBH::08	6.22	-13.04	7/8	0.10	0.0000	0.04976	0.6707	0.3168	0.6768	0.3232	0.9937
EccBBH::09	6.76	-14.17	7/8	0.15	0.0000	0.04472	0.6713	0.3174	0.6768	0.3232	0.9937
EccBBH::10	7.25	-15.21	7/8	0.20	0.0000	0.04036	0.6717	0.3179	0.6768	0.3232	0.9937
EccBBH::11	3.74	-11.19	3/4	0.00	-1.50e-04	0.05548	0.7433	0.2426	0.7500	0.2500	0.9945
EccBBH::12	4.20	-12.61	3/4	0.05	0.0000	0.04893	0.7441	0.2435	0.7500	0.2500	0.9945
EccBBH::13	4.63	-13.92	3/4	0.10	0.0000	0.04363	0.7447	0.2442	0.7500	0.2500	0.9944
EccBBH::14	5.03	-15.13	3/4	0.15	0.0000	0.03919	0.7452	0.2448	0.7500	0.2500	0.9944
EccBBH::15	5.40	-16.24	3/4	0.20	0.0000	0.03537	0.7455	0.2452	0.7500	0.2500	0.9944
EccBBH::16	2.77	-11.49	5/8	0.00	-1.21e-04	0.04762	0.8004	0.1873	0.8062	0.1938	0.9952
EccBBH::17	3.12	-12.96	5/8	0.05	0.0000	0.04193	0.8011	0.1881	0.8062	0.1938	0.9952
EccBBH::18	3.44	-14.32	5/8	0.10	0.0000	0.03736	0.8016	0.1887	0.8062	0.1938	0.9952
EccBBH::19	3.73	-15.57	5/8	0.15	0.0000	0.03354	0.8020	0.1892	0.8062	0.1938	0.9952
EccBBH::20	4.00	-16.70	5/8	0.20	0.0000	0.03027	0.8023	0.1896	0.8062	0.1938	0.9951
EccBBH::21	1.98	-11.51	1/2	0.00	-9.34e-05	0.03952	0.8487	0.1409	0.8536	0.1464	0.9960
EccBBH::22	2.23	-13.00	1/2	0.05	0.0000	0.03474	0.8493	0.1416	0.8536	0.1464	0.9960
EccBBH::23	2.46	-14.37	1/2	0.10	0.0000	0.03091	0.8497	0.1421	0.8536	0.1464	0.9960
EccBBH::24	2.67	-15.62	1/2	0.15	0.0000	0.02774	0.8501	0.1425	0.8536	0.1464	0.9959
EccBBH::25	2.86	-16.74	1/2	0.20	0.0000	0.02503	0.8503	0.1429	0.8536	0.1464	0.9959
EccBBH::26	1.32	-11.23	3/8	0.00	-6.71e-05	0.03109	0.8914	0.1002	0.8953	0.1047	0.9968
EccBBH::27	1.49	-12.70	3/8	0.05	0.0000	0.02727	0.8919	0.1008	0.8953	0.1047	0.9968
EccBBH::28	1.64	-14.05	3/8	0.10	0.0000	0.02423	0.8922	0.1012	0.8953	0.1047	0.9968
EccBBH::29	1.78	-15.26	3/8	0.15	0.0000	0.02173	0.8925	0.1016	0.8953	0.1047	0.9968
EccBBH::30	1.90	-16.34	3/8	0.20	0.0000	0.01962	0.8927	0.1018	0.8953	0.1047	0.9967

TABLE VIII. Properties of the sequence of simulations described in Sec.IV. We report the remnant mass M_f/M and spin χ_f , the radiated energy $\delta\mathcal{M} = M_{\text{ADM}} - M_f$, merger time t_m/M , number of orbits N , strain peak amplitude $(r/M)|h_{22}^{\text{peak}}|$, recoil velocity V_{kick} , peak frequency $M\omega_{22}^{\text{peak}}$ and peak luminosity $\mathcal{L}_{\text{peak}}$.

Run	M_f/M	χ_f	$\delta\mathcal{M}/M$	t_m/M	N	$V_{\text{kick}}[\text{km/s}]$	$(r/M) h_{22}^{\text{peak}} $	$M\omega_{22}^{\text{peak}}$	$\mathcal{L}_{\text{peak}}[10^{-56} \text{ erg/s}]$
EccBBH::01	0.9516	0.6865	0.0415	6081.0	21.37	0.000	0.3940	0.3584	3.6818
EccBBH::02	0.9518	0.6862	0.0412	5617.5	20.14	0.000	0.3929	0.3584	3.6611
EccBBH::03	0.9520	0.6868	0.0410	4787.6	17.77	0.000	0.3930	0.3582	3.6634
EccBBH::04	0.9509	0.6862	0.0421	3736.1	14.58	0.000	0.3954	0.3581	3.7005
EccBBH::05	0.9524	0.6843	0.0407	2640.0	11.21	0.000	0.3880	0.3577	3.5628
EccBBH::06	0.9623	0.6154	0.0315	5990.4	22.00	156.11	0.3387	0.3447	2.7009
EccBBH::07	0.9625	0.6156	0.0312	5550.6	20.66	156.72	0.3390	0.3457	2.7037
EccBBH::08	0.9626	0.6148	0.0311	4649.6	18.01	156.72	0.3371	0.3451	2.6762
EccBBH::09	0.9624	0.6180	0.0313	3530.1	14.64	155.43	0.3431	0.3437	2.7604
EccBBH::10	0.9618	0.6187	0.0319	2395.3	10.83	161.50	0.3454	0.3436	2.8224
EccBBH::11	0.9712	0.5404	0.0232	5930.8	22.45	172.65	0.2863	0.3330	1.8967
EccBBH::12	0.9713	0.5412	0.0232	5477.8	21.35	172.74	0.2875	0.3336	1.9293
EccBBH::13	0.9715	0.5399	0.0230	4537.4	18.35	173.35	0.2847	0.3332	1.8748
EccBBH::14	0.9717	0.5412	0.0227	3384.2	14.60	173.73	0.2848	0.3324	1.8928
EccBBH::15	0.9719	0.5418	0.0225	2233.6	10.61	173.57	0.2849	0.3315	1.8962
EccBBH::16	0.9787	0.4619	0.0165	5720.9	22.92	153.72	0.2341	0.3175	1.2775
EccBBH::17	0.9789	0.4622	0.0163	5253.0	21.36	152.10	0.2355	0.3193	1.2672
EccBBH::18	0.9786	0.4613	0.0166	4289.2	18.14	149.66	0.2348	0.3190	1.2563
EccBBH::19	0.9784	0.4617	0.0167	3124.5	14.30	147.80	0.2359	0.3217	1.2828
EccBBH::20	0.9784	0.4649	0.0168	1975.5	9.81	163.17	0.2395	0.3196	1.3149
EccBBH::21	0.9850	0.3794	0.0110	5495.0	23.57	119.31	0.1855	0.3075	0.7984
EccBBH::22	0.9850	0.3787	0.0109	4977.0	21.67	117.31	0.1849	0.3091	0.7816
EccBBH::23	0.9851	0.3808	0.0108	4002.8	18.17	117.38	0.1873	0.3098	0.8046
EccBBH::24	0.9852	0.3788	0.0107	2826.8	14.07	113.45	0.1838	0.3090	0.7794
EccBBH::25	0.9846	0.3797	0.0113	1639.1	8.91	108.73	0.1870	0.3096	0.8027
EccBBH::26	0.9902	0.2924	0.0066	5283.0	24.40	78.04	0.1373	0.2991	0.4392
EccBBH::27	0.9901	0.2922	0.0067	4687.5	22.15	76.26	0.1374	0.2977	0.4342
EccBBH::28	0.9901	0.2924	0.0067	3625.1	17.95	75.24	0.1376	0.2994	0.4340
EccBBH::29	0.9903	0.2924	0.0064	2419.1	13.10	72.68	0.1368	0.2998	0.4322
EccBBH::30	0.9791	0.2976	0.0176	1210.5	7.21	86.67	0.1431	0.2985	0.4761

- [1] V. Gayathri, J. Healy, J. Lange, B. O'Brien, M. Szczepanczyk, I. Bartos, M. Campanelli, S. Klimenko, C. O. Lousto, and R. O'Shaughnessy, *Nature Astron.* **6**, 344 (2022), arXiv:2009.05461 [astro-ph.HE].
- [2] I. M. Romero-Shaw, P. D. Lasky, and E. Thrane, *Astrophys. J.* **940**, 171 (2022), arXiv:2206.14695 [astro-ph.HE].
- [3] E. O'Shea and P. Kumar, *Phys. Rev. D* **108**, 104018 (2023), arXiv:2107.07981 [astro-ph.HE].
- [4] N. Gupte *et al.*, (2024), arXiv:2404.14286 [gr-qc].
- [5] M. Zeeshan and R. O'Shaughnessy, (2024), arXiv:2404.08185 [gr-qc].
- [6] J. Shapiro Key and N. J. Cornish, *Phys. Rev. D* **83**, 083001 (2011), arXiv:1006.3759 [gr-qc].
- [7] D. J. D'Orazio and J. Samsing, *Mon. Not. Roy. Astron. Soc.* **481**, 4775 (2018), arXiv:1805.06194 [astro-ph.HE].
- [8] B.-M. Hoang, S. Naoz, B. Kocsis, W. Farr, and J. McIver, *Astrophys. J.* **875**, L31 (2019), arXiv:1903.00134 [astro-ph.HE].
- [9] A. Sesana, *Phys. Rev. Lett.* **116**, 231102 (2016), arXiv:1602.06951 [gr-qc].
- [10] S. Vitale, *Phys. Rev. Lett.* **117**, 051102 (2016), arXiv:1605.01037 [gr-qc].
- [11] E. Barausse, N. Yunes, and K. Chamberlain, *Phys. Rev. Lett.* **116**, 241104 (2016), arXiv:1603.04075 [gr-qc].
- [12] M. Bonetti, A. Sesana, E. Barausse, and F. Haardt, *Mon. Not. Roy. Astron. Soc.* **477**, 2599 (2018), arXiv:1709.06095 [astro-ph.GA].
- [13] M. Bonetti, A. Sesana, F. Haardt, E. Barausse, and M. Colpi, *Mon. Not. Roy. Astron. Soc.* **486**, 4044 (2019), arXiv:1812.01011 [astro-ph.GA].
- [14] R. Gold and B. Brügmann, *Phys. Rev.* **D88**, 064051 (2013), arXiv:1209.4085 [gr-qc].
- [15] A. Ramos-Buades, S. Husa, G. Pratten, H. Estellés, C. García-Quirós, M. Mateu-Lucena, M. Colleoni, and R. Jaume, *Phys. Rev. D* **101**, 083015 (2020), arXiv:1909.11011 [gr-qc].
- [16] T. Islam, V. Varma, J. Lodman, S. E. Field, G. Khanna, M. A. Scheel, H. P. Pfeiffer, D. Gerosa, and L. E. Kidder, *Phys. Rev. D* **103**, 064022 (2021), arXiv:2101.11798 [gr-qc].
- [17] J. Healy and C. O. Lousto, *Phys. Rev. D* **105**, 124010 (2022), arXiv:2202.00018 [gr-qc].
- [18] D. Ferguson *et al.*, (2023), arXiv:2309.00262 [gr-qc].
- [19] M. Boschini, N. Loutrel, D. Gerosa, and G. Fumagalli, (2024), arXiv:2411.00098 [gr-qc].
- [20] M. Campanelli, C. O. Lousto, H. Nakano, and Y. Zlochower, *Phys. Rev.* **D79**, 084010 (2009), arXiv:0808.0713 [gr-qc].
- [21] M. A. Shaikh, V. Varma, H. P. Pfeiffer, A. Ramos-Buades, and M. van de Meent, *Phys. Rev. D* **108**, 104007 (2023), arXiv:2302.11257 [gr-qc].
- [22] I. Hinder, L. E. Kidder, and H. P. Pfeiffer, *Phys. Rev. D* **98**, 044015 (2018), arXiv:1709.02007 [gr-qc].
- [23] S. Albanesi, A. Placidi, A. Nagar, M. Orselli, and S. Bernuzzi, *Phys. Rev. D* **105**, L121503 (2022), arXiv:2203.16286 [gr-qc].
- [24] A. Albertini, R. Gamba, A. Nagar, and S. Bernuzzi, *Phys. Rev. D* **109**, 044022 (2024), arXiv:2310.13578 [gr-qc].
- [25] Y. Zlochower, J. G. Baker, M. Campanelli, and C. O. Lousto, *Phys. Rev.* **D72**, 024021 (2005), arXiv:gr-qc/0505055.
- [26] C. O. Lousto and Y. Zlochower, *Phys. Rev.* **D77**, 024034 (2008), arXiv:0711.1165 [gr-qc].
- [27] Y. Zlochower, M. Ponce, and C. O. Lousto, *Phys. Rev.* **D86**, 104056 (2012), arXiv:1208.5494 [gr-qc].
- [28] S. Brandt and B. Brügmann, *Phys. Rev. Lett.* **78**, 3606 (1997), gr-qc/9703066.
- [29] M. Ansorg, B. Brügmann, and W. Tichy, *Phys. Rev.* **D70**, 064011 (2004), gr-qc/0404056.
- [30] J. Thornburg, *Class. Quant. Grav.* **21**, 743 (2004), gr-qc/0306056.
- [31] A. Ashtekar and B. Krishnan, *Living Rev. Rel.* **7**, 10 (2004), gr-qc/0407042.
- [32] M. Campanelli, C. O. Lousto, Y. Zlochower, B. Krishnan, and D. Merritt, *Phys. Rev.* **D75**, 064030 (2007), gr-qc/0612076.
- [33] E. Schnetter, S. H. Hawley, and I. Hawke, *Class. Quant. Grav.* **21**, 1465 (2004), gr-qc/0310042.
- [34] C. O. Lousto and J. Healy, *Phys. Rev. Lett.* **125**, 191102 (2020), arXiv:2006.04818 [gr-qc].
- [35] M. Campanelli, C. O. Lousto, P. Marronetti, and Y. Zlochower, *Phys. Rev. Lett.* **96**, 111101 (2006), gr-qc/0511048.
- [36] J. R. van Meter, J. G. Baker, M. Koppitz, and D.-I. Choi, *Phys. Rev.* **D73**, 124011 (2006), gr-qc/0605030.
- [37] M. Campanelli and C. O. Lousto, *Phys. Rev.* **D59**, 124022 (1999), arXiv:gr-qc/9811019 [gr-qc].
- [38] C. O. Lousto and Y. Zlochower, *Phys. Rev.* **D76**, 041502(R) (2007), gr-qc/0703061.
- [39] H. Nakano, J. Healy, C. O. Lousto, and Y. Zlochower, *Phys. Rev.* **D91**, 104022 (2015), arXiv:1503.00718 [gr-qc].
- [40] H.-S. Cho, E. Ochsner, R. O'Shaughnessy, C. Kim, and C.-H. Lee, *Phys. Rev.* **D87**, 024004 (2013), arXiv:1209.4494 [gr-qc].
- [41] G. Lovelace *et al.*, *Class. Quant. Grav.* **33**, 244002 (2016), arXiv:1607.05377 [gr-qc].
- [42] J. Healy, C. O. Lousto, Y. Zlochower, and M. Campanelli, *Class. Quant. Grav.* **34**, 224001 (2017), arXiv:1703.03423 [gr-qc].
- [43] J. Healy, C. O. Lousto, J. Lange, R. O'Shaughnessy, Y. Zlochower, and M. Campanelli, *Phys. Rev.* **D100**, 024021 (2019), arXiv:1901.02553 [gr-qc].
- [44] J. Healy and C. O. Lousto, *Phys. Rev. D* **102**, 104018 (2020), arXiv:2007.07910 [gr-qc].
- [45] J. Healy, C. O. Lousto, and N. Rosato, *Phys. Rev. D* **102**, 024040 (2020), arXiv:2003.02286 [gr-qc].
- [46] N. Rosato, J. Healy, and C. O. Lousto, *Phys. Rev. D* **103**, 104068 (2021), arXiv:2103.09326 [gr-qc].
- [47] C. O. Lousto and J. Healy, *Class. Quant. Grav.* **40**, 09LT01 (2023), arXiv:2203.08831 [gr-qc].
- [48] E. Schnetter, *Class. Quant. Grav.* **27**, 167001 (2010), arXiv:1003.0859 [gr-qc].
- [49] A. Ciarfella, J. Healy, C. O. Lousto, and H. Nakano, *Phys. Rev. D* **106**, 104035 (2022), arXiv:2206.13532 [gr-qc].
- [50] G. Cho, S. Tanay, A. Gopakumar, and H. M. Lee, *Phys. Rev. D* **105**, 064010 (2022), arXiv:2110.09608 [gr-qc].
- [51] C. K. Mishra and B. R. Iyer, *Phys. Rev. D* **82**, 104005 (2010), [Erratum: *Phys.Rev.D* 84, 069908 (2011), Erra-

- tum: Phys.Rev.D 87, 069906 (2013)], arXiv:1008.4009 [gr-qc].
- [52] P. C. Peters and J. Mathews, Phys. Rev. **131**, 435 (1963).
 - [53] P. C. Peters, Phys. Rev. **136**, B1224 (1964).
 - [54] J. N. Arredondo and N. Loutrel, Class. Quant. Grav. **38**, 165001 (2021), arXiv:2101.10963 [gr-qc].
 - [55] M. Campanelli, C. O. Lousto, and Y. Zlochower, Phys. Rev. **D74**, 084023 (2006), astro-ph/0608275.
 - [56] L. E. Kidder, Phys. Rev. **D52**, 821 (1995), gr-qc/9506022.
 - [57] C. Munna and C. R. Evans, Phys. Rev. D **102**, 104006 (2020), arXiv:2009.01254 [gr-qc].
 - [58] L. Blanchet, Living Rev. Rel. **27**, 4 (2024).
 - [59] D. N. Page, (2024), 10.1103/PhysRevD.110.064062, arXiv:2403.10804 [gr-qc].
 - [60] D. N. Page, JCAP **07**, 017 (2024), arXiv:2405.13673 [gr-qc].
 - [61] J. Healy, C. O. Lousto, J. Lange, and R. O’Shaughnessy, Phys. Rev. D **102**, 124053 (2020), arXiv:2010.00108 [gr-qc].
 - [62] J. Healy, C. O. Lousto, H. Nakano, and Y. Zlochower, Class. Quant. Grav. **34**, 145011 (2017), arXiv:1702.00872 [gr-qc].
 - [63] A. Ciarfella, J. Healy, C. O. Lousto, and H. Nakano, Phys. Rev. D **110**, 084031 (2024), arXiv:2406.11564 [gr-qc].